

1 This is a non-peer-reviewed pre-print of a manuscript
2 which has been submitted for consideration.
3 Manuscript title: Array-based seismic measurements of
4 OSIRIS-REx's re-entry
5 Authors: Fernando, B. et al

Array-based seismic measurements of OSIRIS-REx's re-entry

Benjamin A. Fernando¹, Constantinos Charalambous², Nick Schmerr³, Timothy J. Craig⁴, Jonathan Wolf⁵, Kevin Lewis¹, Eleanor K. Sansom^{6,7}, Christelle Saliby⁸, Meaghan McCleary⁹, Jennifer Inman¹⁰, Justin LaPierre¹¹, Miro Ronac Giannone¹², Karen Pearson¹³, Michael Fleigle¹⁴, Carene Larmat¹⁵, Ozgur Karatekin¹⁶, Lavender Elle Hanson¹, Shivani Baliyan¹⁷, David Buttsworth¹⁸, Hiu Ching Jupiter Cheng¹⁹, Neeraja S. Chinchalkar²⁰, Luke Daly²¹, Hadrien A. R. Devillepoix⁴, Aly Muhammad Gajani²², Carina T. Gerritzen²³, Harish²⁴, Daniel C. Hicks²⁵, Roy Johnson²⁶, Sabrina Y. Khan¹, Sarah N. Lamm²⁷, Cara Pesciotta¹, Tom Rivlin²⁸, Lucie Rolland²⁹, Maxwell Marzban Thiemens³⁰, Alice R. Turner³¹, and Fabian Zander¹⁸

Abstract

The return home of the OSIRIS-REx spacecraft in September 2023 marked only the fifth time that an artificial object entered the Earth's atmosphere at interplanetary velocities. Although rare, such events serve as valuable analogues for natural meteoroid re-entries; enabling study of hypersonic dynamics, shockwave generation, and acoustic-to-seismic coupling. Here, we report on the signatures recorded by a dense (100-m scale) 11-station array located almost directly underneath the capsule's point of peak atmospheric heating in northern Nevada. Seismic data are presented which allow inferences to be made about the shape of the shockwave's footprint on the surface, the capsule's trajectory, and its flight parameters.

Cite this article as Fernando, B. et al (2022). Array-based seismic measurements of OSIRIS-REx's re-entry, *Seismol. Res. Lett.* **XX**, 2–12, doi: 00.0000/0000000000.

[Supplemental Material](#)

1. Department of Earth and Planetary Sciences, Johns Hopkins University, Baltimore, Maryland, United States, <https://orcid.org/0000-0002-7321-8401> BF, <https://orcid.org/0000-0003-3412-803X> KL, <https://orcid.org/0000-0003-2298-8382> LEH, <https://orcid.org/0000-0003-4212-4848> SK, <https://orcid.org/0009-0007-6910-6347> CP; 2. Department of Electrical and Electronic Engineering, Imperial College London, London, United Kingdom, <https://orcid.org/0000-0002-9139-3895> CC; 3. Department of Geology, University of Maryland, College Park, Maryland, United States, <https://orcid.org/0000-0002-3256-1262> NS; 4. Institute of Geophysics and Tectonics, School of Earth and Environment, University of Leeds, Leeds, United Kingdom, <https://orcid.org/0000-0003-2198-9172> TC; 5. Department of Earth and Planetary Sciences, University of California, Berkeley, California, United States, <https://orcid.org/https://orcid.org/0000-0002-5440-3791> JW; 6. International Centre for Radio Astronomy Research, Space Science and Technology Centre, Curtin University, Perth, Western Australia, Australia, <https://orcid.org/0000-0003-2702-673X> ES, <https://orcid.org/0000-0001-9226-1870> HD; 7. Space Science and Technology Centre, School of Earth and Planetary Science, Curtin University, Perth, Australia, <https://orcid.org/0000-0003-2702-673X> ES; 8. Observatoire de la Côte d'Azur, Université Côte d'Azur, CNRS, IRD, Géoazur, Valbonne, France, <https://orcid.org/0000-0002-0101-723X> CS; 9. Analytical Mechanics Associates, Inc./NASA Langley Research Center, Hampton, Virginia, United States, <https://orcid.org/0009-0008-5233-2820> MM; 10. NASA Langley Research Center, Hampton, Virginia, United States, <https://orcid.org/0000-0001-6213-3181> JI; 11. Sandia National Laboratories, Albuquerque, New Mexico, United States, <https://orcid.org/0000-0001-9377-6331> JL; 12. Department of Earth Sciences, Southern Methodist University, Dallas, Texas, United States, <https://orcid.org/0000-0001-8752-2263> MRG; 13. Independent Researcher, Bowie, Maryland, United States, KP; 14. Sandia National Laboratories, Albuquerque, New Mexico, United States, MF; 15. Los Alamos National Laboratory, New Mexico, United States, <https://orcid.org/0000-0002-3607-7558> CL; 16. Royal Observatory of Belgium, Uccle, Belgium, <https://orcid.org/0000-0003-0153-7291> OK; 17. Independent Researcher, Boulder, Colorado, United States, <https://orcid.org/0000-0001-9475-0870> SB; 18. Institute for Advanced Engineering and Space Sciences, University of Southern Queensland, Queensland, Australia, <https://orcid.org/0000-0001-6787-9580> DB, <https://orcid.org/0000-0003-0597-9556> FZ; 19. Department of Geological Sciences, University of Alabama, Tuscaloosa, Alabama, USA, <https://orcid.org/0000-0002-0883-5059> JC; 20. University of Western Ontario, London, Ontario, Canada, <https://orcid.org/0000-0002-3541-3791> NC; 21. School of Geographical and Earth Sciences, University of Glasgow, Glasgow, United Kingdom, <https://orcid.org/0000-0002-7150-4092> LD; 22. Institute of Space Science and Technology, University of Karachi, Karachi, Pakistan, <https://orcid.org/0009-0001-5249-9873> AMG; 23. Archaeology, Environmental Changes & Geo-Chemistry, Vrije Universiteit Brussel, Brussels, Belgium, <https://orcid.org/0000-0002-1494-2643> CTG; 24. Laboratory for Atmospheric and Space Physics, University of Colorado, Boulder, Colorado, United States, <https://orcid.org/0000-0002-4152-4295> H; 25. United States Department of Defense (KBR Consultant), Las Cruces, New Mexico, United States, DCH; 26. NASA Ames Research Center, Moffett Field, California, United States, <https://orcid.org/0009-0008-9028-9843> RJ; 27. Earth, Energy, and Environment Centre, University of Kansas, Lawrence, Kansas, United States, <https://orcid.org/0000-0003-3810-1213> SNL; 28. Atominstytut, Technische Universität Wien, Vienna, Austria, <https://orcid.org/0000-0002-9275-2917> TR; 29. Laboratoire Géoazur - Université de Nice Côte d'Azur, <https://orcid.org/0000-0002-5197-963X> LR; 30. Department of Geosciences, University of Edinburgh, Edinburgh, Scotland, <https://orcid.org/0000-0002-7835-4402> MMT; 31. Institute for Geophysics, University of Texas, Austin, Texas, United States, <https://orcid.org/0000-0002-3743-6428> ART

0002-3607-7558 CL; 16. Royal Observatory of Belgium, Uccle, Belgium, <https://orcid.org/0000-0003-0153-7291> OK; 17. Independent Researcher, Boulder, Colorado, United States, <https://orcid.org/0000-0001-9475-0870> SB; 18. Institute for Advanced Engineering and Space Sciences, University of Southern Queensland, Queensland, Australia, <https://orcid.org/0000-0001-6787-9580> DB, <https://orcid.org/0000-0003-0597-9556> FZ; 19. Department of Geological Sciences, University of Alabama, Tuscaloosa, Alabama, USA, <https://orcid.org/0000-0002-0883-5059> JC; 20. University of Western Ontario, London, Ontario, Canada, <https://orcid.org/0000-0002-3541-3791> NC; 21. School of Geographical and Earth Sciences, University of Glasgow, Glasgow, United Kingdom, <https://orcid.org/0000-0002-7150-4092> LD; 22. Institute of Space Science and Technology, University of Karachi, Karachi, Pakistan, <https://orcid.org/0009-0001-5249-9873> AMG; 23. Archaeology, Environmental Changes & Geo-Chemistry, Vrije Universiteit Brussel, Brussels, Belgium, <https://orcid.org/0000-0002-1494-2643> CTG; 24. Laboratory for Atmospheric and Space Physics, University of Colorado, Boulder, Colorado, United States, <https://orcid.org/0000-0002-4152-4295> H; 25. United States Department of Defense (KBR Consultant), Las Cruces, New Mexico, United States, DCH; 26. NASA Ames Research Center, Moffett Field, California, United States, <https://orcid.org/0009-0008-9028-9843> RJ; 27. Earth, Energy, and Environment Centre, University of Kansas, Lawrence, Kansas, United States, <https://orcid.org/0000-0003-3810-1213> SNL; 28. Atominstytut, Technische Universität Wien, Vienna, Austria, <https://orcid.org/0000-0002-9275-2917> TR; 29. Laboratoire Géoazur - Université de Nice Côte d'Azur, <https://orcid.org/0000-0002-5197-963X> LR; 30. Department of Geosciences, University of Edinburgh, Edinburgh, Scotland, <https://orcid.org/0000-0002-7835-4402> MMT; 31. Institute for Geophysics, University of Texas, Austin, Texas, United States, <https://orcid.org/0000-0002-3743-6428> ART

*Corresponding author: bfernan9@jh.edu

© Seismological Society of America

6 Introduction

7 Sample return capsules and seismoacoustics

8 Sample return capsules arriving from deep space are the
9 only artificial objects which re-enter the Earth's atmosphere
10 at speeds and trajectories comparable to natural meteoroids.
11 This makes them ideal for studying hypersonic re-entry
12 dynamics as said capsules have known mass, dimension,
13 speed, and trajectory (Silber et al., 2023). Because they have
14 known parameters, they can serve as controlled analogues
15 for natural objects during the EDL (Entry, Descent, and
16 Landing) phase of the mission.

17 In seismoacoustic studies of meteor phenomena, the
18 atmospheric shockwaves and low-frequency sound pro-
19 duced by natural meteoroids re-entering the atmosphere are
20 used to identify and track them on either infrasound sensors
21 or seismometers (e.g. Edwards et al. (2008)). The complexi-
22 ties of shockwave generation and propagation down through
23 the turbulent atmosphere (and coupling into the ground
24 in the case of seismic recordings) mean that recordings
25 of hypersonic capsules acting as 'artificial meteoroids' are
26 particularly valuable in understanding the seismoacoustic
27 processes involved.

28 Such events are rare, having occurred only four times on
29 Earth previously. ReVelle et al. (2005) made seismic and
30 acoustic measurements of NASA's Genesis spacecraft's EDL,
31 and ReVelle and Edwards (2007) did the same for NASA's
32 Stardust. More recently, comparable measurements were
33 made during the EDLs of two JAXA missions, Hayabusa and
34 Hayabusa2 (Yamamoto et al., 2011; Sansom et al., 2022).

35 The potential value of such recordings for being able to
36 study shockwave propagation and air-to-ground coupling in
37 particular also resulted in two (unsuccessful) attempts by
38 NASA's InSight spacecraft to record EDLs seismoacousti-
39 cally on Mars, of NASA's Mars 2020 mission (Fernando et al.,
40 2021, 2022) and China's Tianwen-1 (Fernando et al., 2021).

41 The OSIRIS-REx mission

42 In September 2023, the OSIRIS-REx (ORX) sample return
43 capsule became the fifth artificial object to re-enter the
44 Earth's atmosphere at interplanetary speeds. With many
45 improvements in instrumentation having been made since
46 Stardust's landing in 2006, the ORX EDL presented an ideal
47 opportunity to make seismoacoustic measurements of an
48 'artificial meteoroid' re-entry over a similar geographical
49 area to two previous missions.

50 A number of different teams took part in this instrumenta-
51 tion campaign, using both ground-based and airborne infra-
52 sound sensors, and conventional and optical seismometers.
53 For a full review of the instruments deployed as part of
54 this campaign see Silber et al. (2024). Fernando et al. (2024)
55 presented initial results from a separate part of this observa-
56 tion campaign, using a single seismic-acoustic station from
57 which the data was live-streamed over the internet.

EDL profile

58 In this section, we briefly describe the planned trajectory of
59 ORX between atmospheric interface and peak heating. Note
60 that all times and locations are based on pre-landing model
61 predictions (e.g. Ajluni et al. (2015)), as a post-landing 'as-
62 flown' trajectory has not yet been released.
63

64 Atmospheric interface was due to occur over the Pacific
65 Ocean, west of San Francisco, California at 14:41:55 UTC
66 on Sunday, 2023-09-24. The defined altitude of interface
67 was 132 km, at which time the spacecraft was expected
68 to be travelling at approximately Mach 25 (43,000 km/h;
69 11.9 km/s).

70 At the point of peak atmospheric heating from frictional
71 drag, the capsule was expected to be in the mesosphere
72 at around 62 km altitude over 39.5585°N, 116.3852°W in
73 northern Nevada. This is a relatively remote region with no
74 permanent seismometers within several dozen kilometres,
75 and we are not aware of any publicly accessible infrasound
76 stations within the wider area. This necessitated deploy-
77 ment of these temporary seismic arrays.

78 Temperatures during peak heating were expected to reach
79 approximately 3100 K at a speed of Mach 30 (39,000 km/h;
80 10.8 km/s) and a deceleration approaching 300 m/s² (31 g).
81 Note that the Mach number at peak heating is actually
82 higher than at atmospheric interface despite the capsule's
83 deceleration, due to the increase in sound speed with alti-
84 tude through the thermosphere.

85 As the point of peak heating is where the maximum
86 amount of energy is being dissipated into the atmosphere,
87 the expectation was for an intense shockwave to be gener-
88 ated in this area. This shock was expected to transition to a
89 linear acoustic wave during propagation down through the
90 atmosphere and be audible at the surface as a sonic boom.

91 On a seismic network, the sonic booms themselves are
92 primarily recorded via the production of an itinerant strain
93 field in response to the surface loading and unloading from
94 wavefront-induced compression and rarefaction (Kanamori
95 et al., 1992). Small contributions to the observed displace-
96 ment after the initial motion may also come about from
97 more complex effects, such as compliance-induced ground
98 deformation (Sorrells, 1971; Kenda et al., 2020).

Instrumentation campaign

99 The deployment discussed in this paper involved eleven
100 individual seismic stations, each consisting of a three-axis
101 Fairfield ZLand 3C Nodes set to 24dB gain and 2000 samples
102 per second.
103

104 The deployment location for these nodes was chosen to be
105 as close to the point of projected peak heating as possible, to
106 try to capture the shockwave at its strongest point. For nat-
107 ural meteoroids, peak emission is expected to occur around
108 the point of peak heating, and hence measurements made

of artificial capsules in this region of flight are of particular interest as analogues.

The array was located at Bean Flats, on United States Bureau of Land Management land, in an area shared with large herbivorous creatures (cows). Despite the presence of topographic variation in the wider region, this area itself was very flat, with less than 4 m of undulation between the array's centre and edge in any direction. Given a sound-speed in air of approximately 330 m/s, this corresponds to a very small elevation-induced correction to phase arrival times, on the order of 0.01 s.

Instruments were deployed in a cross-shaped array, with an instrument spacing of approximately 100 m. This configuration, and wider geographical context, are shown in Fig. 1 alongside the ORX EDL trajectory. The long axis of the array was chosen to be parallel to ORX's trajectory footprint.

Each instrument was manually levelled and pointed toward north using multiple compasses as references, with errors in orientation estimated to be less than $\pm 2^\circ$. The reported GPS coordinates of each station are the mean of readings made on multiple handheld instruments.

The sensors were buried with their tops a few centimetres below the ground's surface to reduce environmental noise. Some of the surface covering was removed by rain and wind (and possibly the actions of the previously mentioned herbivores) between deployment and collection. In particular, signals from instrument 4 (the most uprange) were found to be particularly noisy. The ground at this location was ascertained to be soft, mostly dry superficial alluvium. Detailed geophysical surveys from this area of Nevada suggest soil properties described by $V_p = 585$ m/s and $V_s = 350$ m/s, Poisson ratio $\nu = 0.22$, and Young's Modulus $E = 0.45$ MPa (Allander and Berger, 2009).

Seismic data

Data were recorded at all eleven stations, and are shown in Fig. 2. Seismograms were processed by removing the instrument response and Butterworth-bandpass filtering between 1 and 100 Hz. The beam shown in 4 uses a slightly broader frequency range, 2 to 200 Hz.

Detailed N-wave structure

A clear, rounded (smoothed) N-wave signature is observed just after 14:46:04.5 UTC. A downwards, near-instantaneous first motion associated with the acoustic compression is followed by an upwards ground motion associated with the atmospheric rarefaction.

The rounding of the N-wave is characteristic of a shock-wave which has decayed in the turbulent atmosphere (in particular the planetary boundary layer) to become a linear sound wave, though retaining its characteristic N-wave shape in a more rounded form (Ben-Menahem and Singh, 1981; Plotkin, 2002; Pierce and Maglieri, 1972). The arrival

time is commensurate with the expected capsule overflight a few minutes previously (around 14:42 UTC). The overall duration of the N-wave phase within the wavetrain is around 0.20-0.25 s, depending on which station is examined and how the end of the rarefaction period is chosen (we use the first zero-crossing after the rarefaction).

Differences are observed in the structure of the rounded N-wave (Fig. 2), even between stations which are separated by only 100 m. Frequencies up to 500 Hz are recorded at some stations (e.g., 2 and 10), while others (e.g., 1 and 3) are limited to highest frequencies around 400 Hz. The rarefaction has a narrower frequency content than the compression, and is accordingly broader.

The most significant origins of these differences are likely propagation effects associated with inhomogeneity and turbulence in the atmosphere (Pierce and Maglieri, 1972) and local variations in sediment properties (causing different coupling behaviour, McDonald and Goforth (1969)). The spatially varying nature of the seismic source itself (i.e., the fact that the capsule is descending and decelerating over time) may also have had a small effect.

We now consider a more detailed analysis of the signal recorded at a single station, as shown in Fig. 3. These data are for station 1, as it is located at the array centre, but similar features are recorded across the array.

As per Fig. 3A), the N-wave is most clearly detectable on the vertical component, as is expected for a wavefront travelling almost vertically downward (McDonald and Goforth, 1969).

Fig. 3B) shows a vertical component spectrogram. Weak background noise, with energy predominantly at frequencies up to 30 Hz, is apparent before the rounded N-wave arrival. The amplitude variations across the array (higher noise levels closer to the road), the move-out of the energy, and the identification of similar signatures in the seismic record at a later time (15:25-15:27 UTC) collectively indicate a vehicular origin for this particular noise source. This is discussed further in the *Traffic* section.

Finally, Fig. 3C) shows the ground particle motion associated with the initial N-wave (orange) and the rest of the wavetrain (blue). The overwhelmingly vertical motion associated with the N-wave is clear. A potential elliptical polarisation can be seen in the rest of the wavetrain, suggesting the presence of Rayleigh waves here.

Slowness and origin azimuth

In considering the passage of the sonic boom over the array, it is important to consider that the capsule does not act as a point source. Rather, whilst travelling at supersonic speeds it is more appropriately described as a line source producing a conical shock front (Carlson and Maglieri, 1972). The opening angle of the cone, μ , is given by:

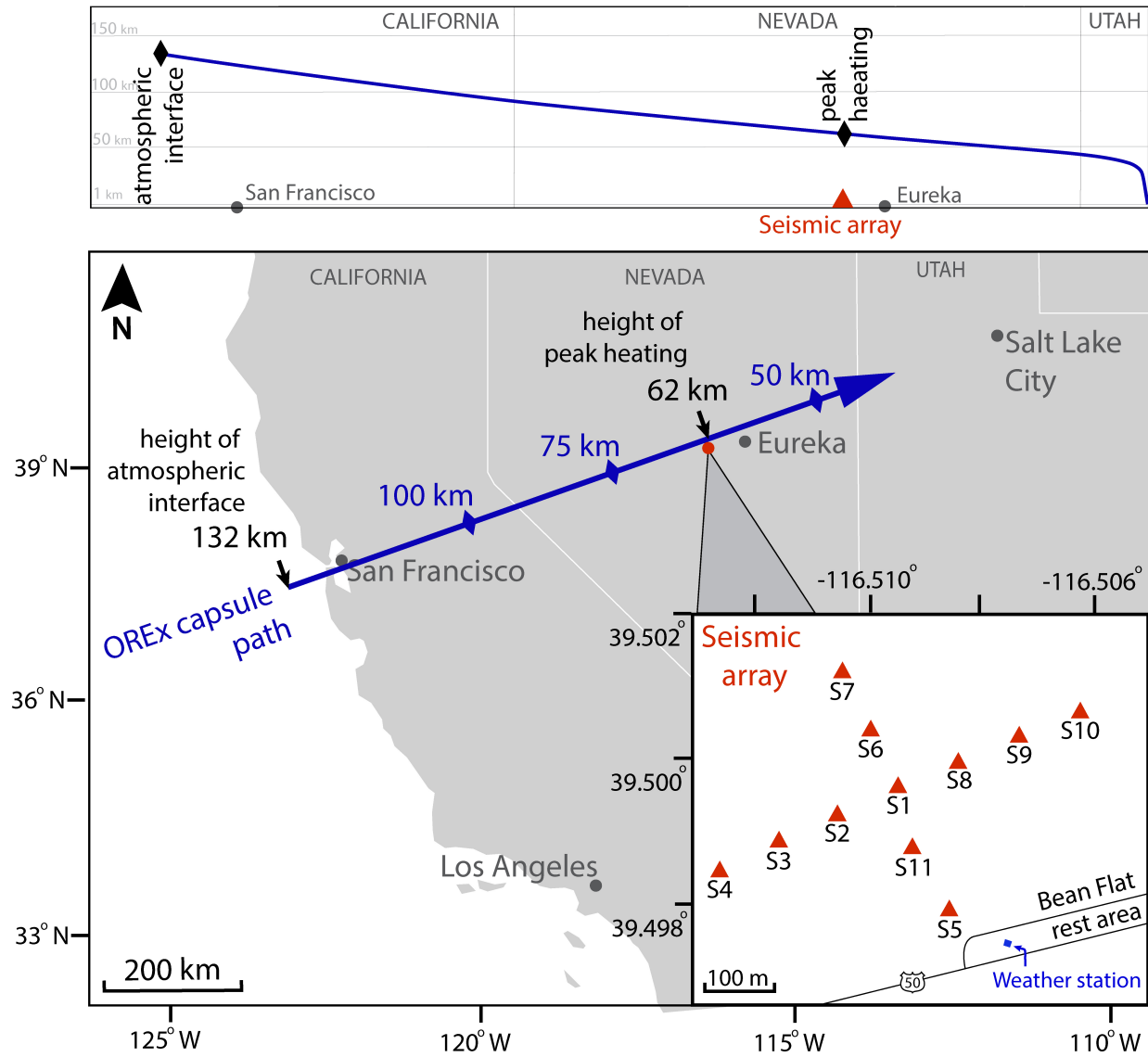


Figure 1. Top panel: the ORX EDL trajectory (side view), from the point of atmospheric interface to landing. Bottom panel: geographical context (top-down view) of the trajectory. We refer to directions towards landing as ‘downrange’ and those towards atmospheric interface as ‘uprange’. The inset panel shows the seismometer array deployment. Note that the long

arm of the array is parallel to the expected trajectory (i.e. runs uprange/downrange). The cross arm is perpendicular to the trajectory (i.e. crossrange). The lateral distance between the centre-line of the array and the trajectory footprint on the ground is approximately 2300 m.

$$\mu = \arcsin \frac{1}{M} \quad (1)$$

where M is the Mach number, in this case 30 – corresponding to an opening angle of 1.9° . This narrow Mach cone means that the seismic source may effectively be considered to be a cylinder (Karakostas et al., 2018). The acoustic rays themselves are emitted at the complement of the Mach angle (Cates and Sturtevant, 2002), which in this case is 88.1° , i.e., nearly normal to the shock front.

The intersection of the Mach cone with the ground produces a hyperbola along which a sonic boom is audible, and

the passage of the hyperbola over the surface sweeps out a sonic boom ‘carpet’. As per Eqn. 1, the hyperbolic footprint also becomes narrower with increasing Mach number.

In Figure 4, we first show the results of a beampack aimed at determining the 2D slowness of the overpressure wavefront, followed by vespagrams showing beams in slowness s_x and s_y space. These are constructed under the assumption that the wave propagates across the array as a plane wave at consistent velocity. We do not find it necessary to compensate for the small variation in topographic elevation across

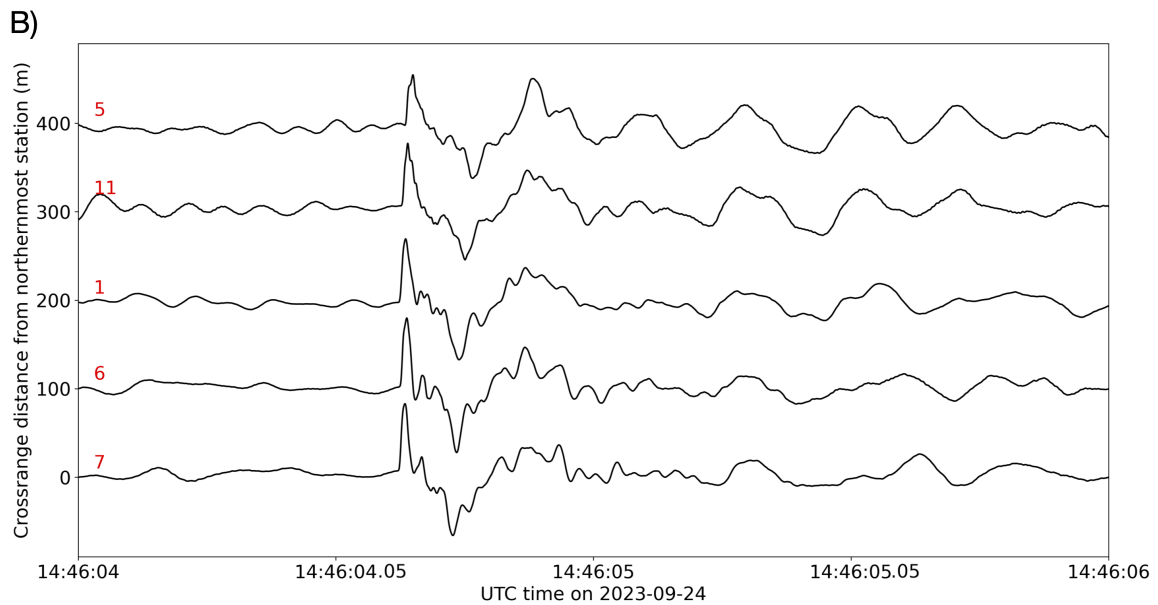
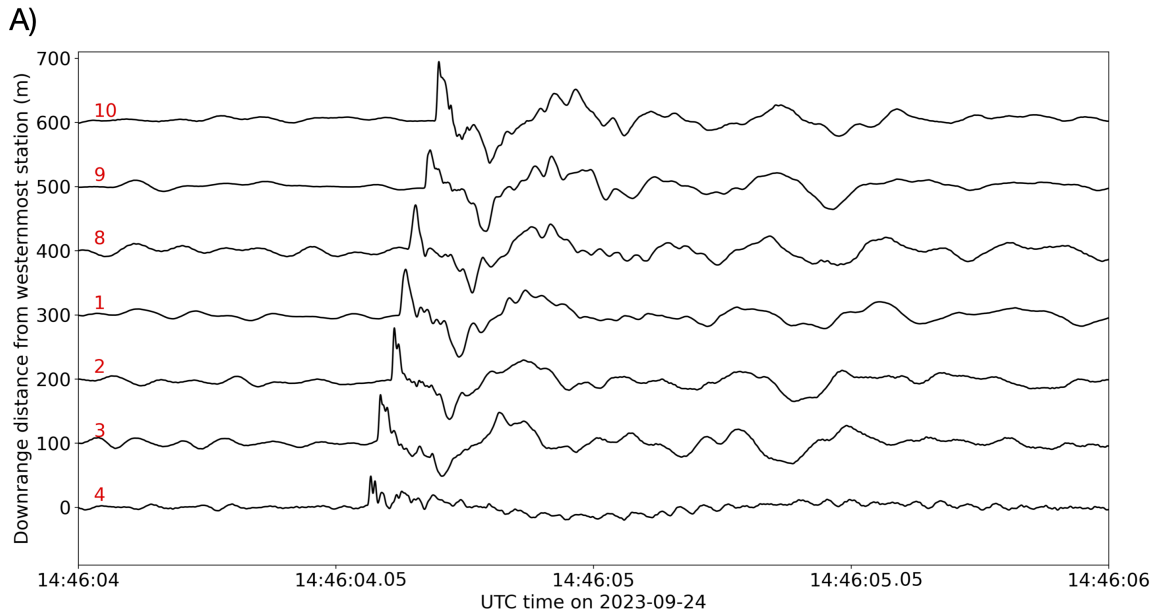


Figure 2. Seismic data recorded by the array. Traces are vertical ground velocity in the 1-100 Hz range and are arranged in **A)** by downrange distance from the westernmost station in the arra and in **B)** by cross-range distance from the

northernmost station. Station numbers are indicated in red on the left hand side. The weak signal at station 4 is thought to be due to issues with the instrument, which displayed higher noise levels throughout the deployment.

231 the array as this is < 4 m across an array aperture of ~ 600 m
232 and hence the impact of elevation variation is small.

233 The beampack shows the maximum arrival amplitude
234 with a 0.025 s window around the overall maximum ampli-
235 tude stack, as a function of slowness in east (s_x) and north
236 (s_y) directions. As Figure 4**A,B)** shows, there is a clear peak
237 in amplitude associated with wavefront arrival at a slowness
238 of $[s_x, s_y] = [-0.209, -0.063]$. The actual signal is convolved

239 with an array response function leading to amplitude arte-
240 facts associated with the orientation of the arms of the array
241 in the uprange and crossrange directions, these are visi-
242 ble as bright lines in the beampack. The fact that the array
243 response function passes slightly northwest of $[0,0]$ in slow-
244 ness space indicates the array was slightly to the south of the
245 actual re-entry trajectory (consistent with pre-landing pre-

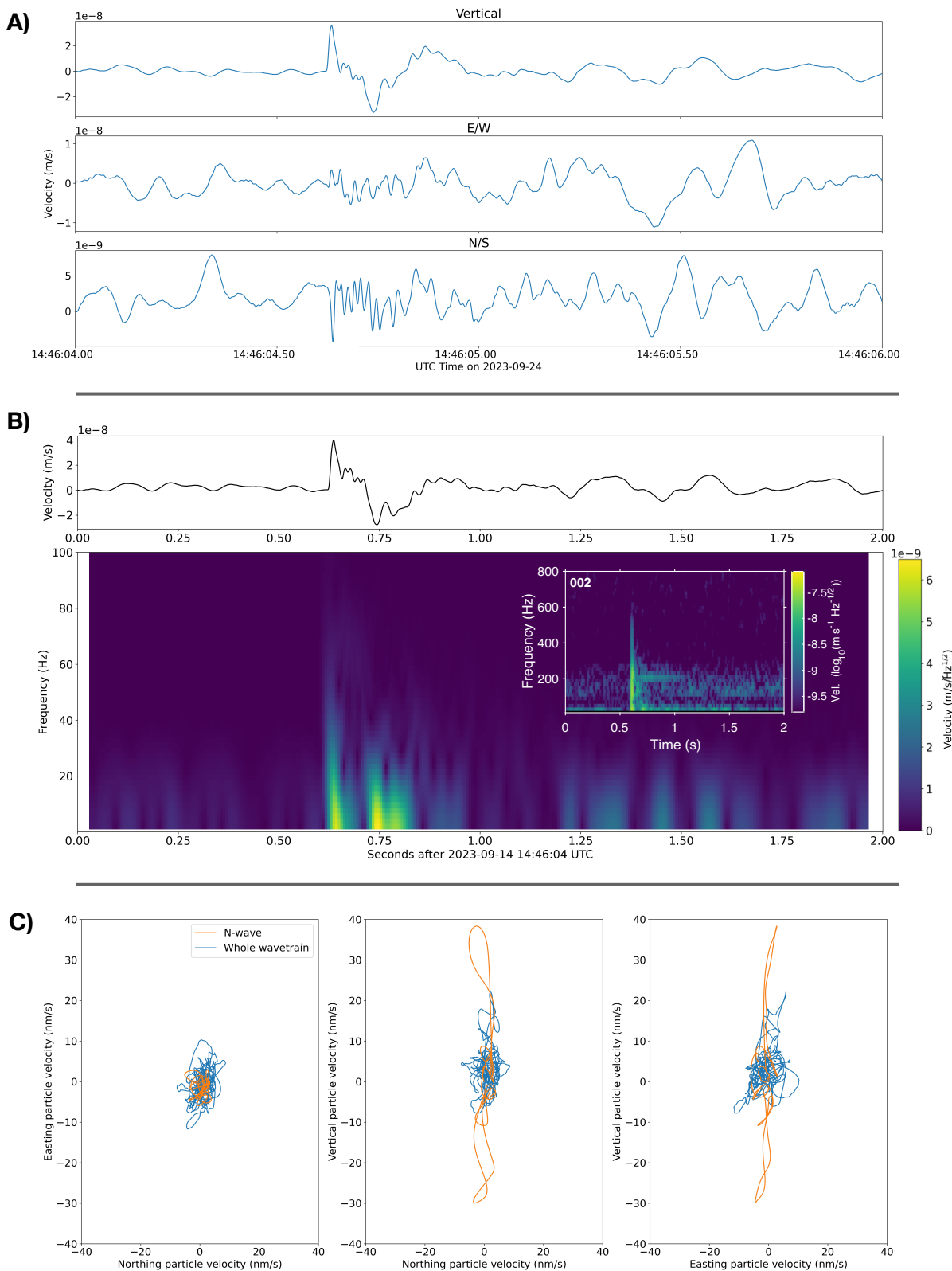


Figure 3. Data from the central station of the array (Station 1), bandpassed between 1 and 100 Hz. The N-wave is only clearly apparent on the vertical component. **A)** Three-component data, showing the dominance of the signal on the vertical component. A small inset is shown for station 2 (one station uprange from station 1), to illustrate the variation in peak

frequency recorded between different stations. At station 2, a resonance around 200 Hz is also observed, which could correspond to excitation in a thin playa layer around 1-2 m thick. **B)** Velocity spectrogram for the vertical component. **C)** Particle motion, with the N wave shown in orange (14:46:04.4 - 14:46:04.8 UTC) and the remainder of the wavetrain in blue.

246 ditions, and indicating that the spacecraft was either on or
247 ever so slightly south of its nominal re-entry line).

248 The 2D slowness of the wavefront arrival indicates that
249 the point of apparent wavefront emission is at an azimuth
250 of 253° (roughly WSW), and an apparent slowness of
251 0.214 s/km. The derived azimuth is very close to the pre-
252 landing nominal prediction of 249°. The beampacked is
253 extremely well resolved, given the frequency of the over-
254 pressure wave and array aperture. The vespagrams in Figure
255 **4C,D**) show evidence for either a slight variation in slowness
256 across the array, or equivalently, the detection of wavefront
257 curvature. In this case, where source-array distance is likely
258 to be only around two orders of magnitude higher than
259 the array aperture, slight wavefront curvature is more likely
260 than the impact of a consistent atmospheric gradient on the
261 lengthscale of the array aperture. The latter would also be
262 expected given that the sonic boom footprint on the ground
263 is a hyperbola.

264 Source location analysis

265 Given the azimuth and slowness resolution of the array,
266 we are also able to estimate origin location of the shock-
267 wave. Without a full atmospheric model and inversion of the
268 data, which are beyond the scope of this paper, this involves
269 making a number of assumptions.

270 Firstly, we assume that the sonic boom can be repre-
271 sented as a plane wave propagating through the atmosphere,
272 which, as we justify above, is an approximation which is
273 reasonable in the far-field. Secondly, we assume that the
274 shockwave has decayed sufficiently such that it propagates
275 at the speed of sound v_0 , which we calculate to be 332 m/s
276 (see *Weather* section for more details on this calculation).

277 Geometrically, we consider the apparent slowness ($s_{app} =$
278 $\frac{1}{v_{app}}$) of the wavefront across the array (e.g. [Rost and Thomas](#)
279 [\(2002\)](#)) as:

$$280 s_{app} = \frac{\sin\theta}{v_0} \quad (2)$$

281 In the downrange direction, the apparent velocity v_{app} of
282 the wavefront across the array is 4,581 m/s. Note that this
283 is an apparent, rather than physical, velocity and yields an
284 estimated angle of emission which is 4.15° from the vertical.
285 This is the equivalent point-source angle of emission, and
286 does not reproduce the actual, extended-line source nature
287 of the capsule as a seismic source; but it does indicate that
288 the signal was produced almost exactly overhead the array,
289 as expected. When combined with the derived bearing from
290 the previous section of 253°, this indicates an origin for
291 the shockwave which is slightly to the south-west of the
292 array and almost vertically above it. Note that this result
293 also suggests that the effects of atmospheric refraction of the
294 acoustic rays is minimal, as each different layer of the verti-

cally stratified atmosphere is encountered at a near-normal
angle to its interface.

Pre- and post-cursors

297 Similarly to [Fernando et al. \(2024\)](#), no clear pre-cursor
298 phases are noted, and there are no coherent sources detected
299 by our array. This is as expected, because pre-cursors
300 are normally restricted to settings where the supersonic
301 source is 'slow' as compared to the compressional speed in
302 the ground, such that surface waves induced immediately
303 beneath the source can 'overtake' a slower direct airwave
304 due to the higher wave speeds in the ground ([Cook and](#)
305 [Goforth, 1970](#)). In this case, the capsule's velocity is very
306 much greater than V_p , thus explaining the absence of pre-
307 cursor phases ([McDonald and Goforth, 1969](#)). Furthermore,
308 the sound speed in the ground is only slightly higher (less
309 than factor 2) than the sound speed in the air.

310 We do note that there is an increase in noise levels around
311 14:45:50 UTC, around twenty seconds before the ORX sig-
312 nal (see *Traffic* section for more details). We exclude this as
313 being a pre-cursor, as it arrives too early as compared to the
314 airwave and has a move-out consistent with a vehicular ori-
315 gin, specifically a lorry/truck that arrived at the nearby rest
316 area and idled until 14:47 UTC.

317 Conversely, a relatively rich set of seismic waves is appar-
318 ent immediately after the initial rounded N-wave. These
319 are visible as an extended set of oscillations in [Figs. 2A\)](#)
320 [and B\)](#). These have similar slowness to the airwave arrival,
321 and hence are potentially associated with acoustic waves
322 propagating in the atmosphere after the initial compres-
323 sion/rarefaction, or longer-duration complex deformation
324 associated with the wavefront's passage over the station. It is
325 also likely that Rayleigh waves are present in this wavetrain.
326 Given that V_s in play is extremely close to the sound-speed
327 in air, the air-to-ground coupling should be strong. However,
328 this closeness of speeds also makes phase separation chal-
329 lenging.

Comparison to known flight parameters

330 In theory, the detailed seismic recordings made at this array
331 could be inverted for the capsule's trajectory and flight
332 parameters. However, this is extremely challenging in prac-
333 tice, due to the lack of an exact atmospheric state model or
334 an as-flown trajectory.

335 Nonetheless, we note that a comparison of the boom
336 duration (τ) to theoretical predictions given by [Kanamori](#)
337 [et al. \(1992\)](#) is possible. Following the approach of [Whitham](#)
338 [\(1974\)](#) (though with slightly different notation, and cor-
339 rection for a missing exponent noted by [Kanamori et al.](#)
340 [\(1992\)](#)), given a capsule speed u at height h we expect τ to
341 be approximately given by:

$$342 \tau \approx \frac{2\sqrt{2k_1k_2}h^{\frac{1}{4}}}{u} \quad (3) \quad 344$$

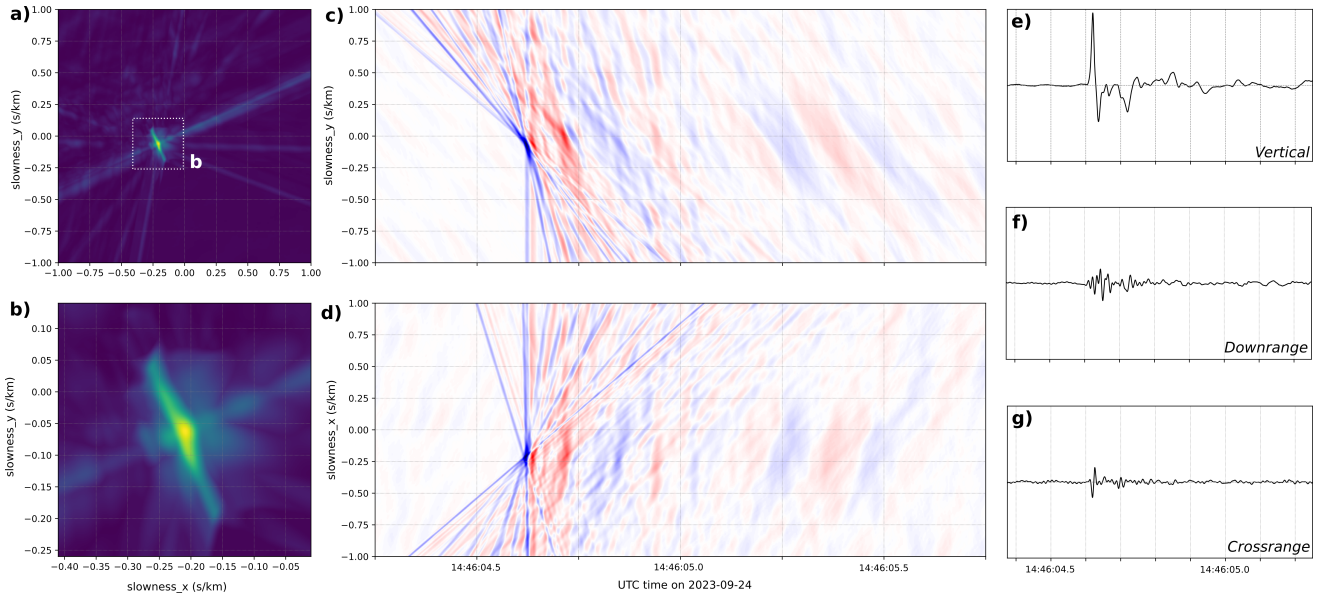


Figure 4. Array analysis of the ORX re-entry signal. (a) and (b) show the results of a beampack through slowness in x and y, taking the maximum amplitude with +/- 50 samples (0.025 seconds) of the absolute maximum amplitude for the shockwave arrival (at 14:46:04.621 and at a slowness of [-0.209, -0.063]). (c) and (d) show vespagrams in y and x slowness space, respectively. In each vespagram, the other

slowness is fixed at the value giving the absolute maximum amplitude for the shockwave arrival. All plots are normalised to the peak value. (e)-(g) show the optimal-slowness beam for vertical, downrange and crossrange components, respectively in pass band 1 – 100 Hz. All beams are normalised to the peak value of the vertical component beam.

where k_1 is a constant dependent on the ratio of specific heats within the atmosphere γ and the Mach number M :

$$k_1 = \frac{(\gamma + 1)M^4}{\sqrt{2}(M^2 - 1)^{\frac{3}{4}}} \quad (4)$$

and k_2 is a constant related to the capsule's geometry,

$$k_2 = \delta l^{\frac{3}{4}} \quad (5)$$

where δ is the ratio of maximum effective capsule radius to capsule length.

For the ORX capsule with radius 0.4 m and length 0.5 m, $k_2 = 0.48$ (noting that in practice, the effective radius of the capsule may be larger due to shockwave stand-off).

Given the nominal pre-landing predictions of $h = 62,000$ m and $u = 10,800$ m/s, and assuming a canonical $\gamma = 1.4$ (as per Kanamori et al. (1992), though it is likely lower at $M = 30$), we derive $k_1 \approx 47,500$. Using the 'effective' (slant) height makes little difference to this calculation given that the capsule is almost directly overhead.

These results yield an estimate of $\tau = 0.43$ s. This is in remarkably close agreement with our measured value of 0.20-0.25 s given the significant simplifications made in the calculation of the constants above and the unknown capsule height and atmospheric conditions at the time of overflight.

Ancillary data

We will briefly discuss ancillary data which was collected as part of this deployment by part of a team of volunteers, working remotely with data provided online by the Nevada Department of Transport (NVDOT). All of this data, and similar readings from nearby potentially of interest to other portions of the ORX EDL instrumentation campaign, are available in our online repository (see Data and Resources section for link).

Weather data

The proximity of the array to US Highway 50 ('The Loneliest Road in America') had the advantage that meteorological data could be sourced from a nearby NVDOT weather station. This station ('US50 Bean Flats Rest Area') was only 275 m from the array centrepoint. The closest reading to the capsule's overflight and the arrival of the sonic boom was made at 14:44:00 UTC, with measurements shown in Table 1.

Whilst the lack of wind during this period represents only a single measurement at the surface, it may be indicative of a quiescent planetary boundary layer at the time in question. This may have led to less turbulent dissipation of the wavefront (one of the sources of rounding in the N-wave).

TABLE 1.
Meteorological data recorded by the Nevada Department of Transport Weather Station at US 50 Bean Flats Rest Area at 14:46:00 UTC. Data are shared as provided, surface temperature has been averaged over two sensors.

Variable	Value
Air temperature	+4.5°C
Surface temperature	+8.2°C
Dewpoint	-3.3°C
Relative humidity	56%
Wind direction	302°
Wind speed	0.0 m/s
Gust direction	291°
Gust speed	0.22 m/s
Precipitation	None

Traffic data

We also made use of the traffic camera installed at the Bean Flats Rest area to record traffic movements, with the aim of being able to identify contamination in the ORX signal if needed.

Data for around five minutes before and after the overflight are given in Table 2. Because the traffic camera feeds are not archived, multiple volunteers were asked to record vehicles passing the array, thereby eliminating some of random the error associated with streaming lag (we find a systematic error of around 40 s delay in video data as compared to when a vehicle becomes apparent in the seismic data). The data provided is a synthesis of that from all volunteers, with the lower, mean, and upper bounds on vehicle passage times given. The streaming lag has not been corrected for in 2.

In two cases, the vehicle may have been towing a trailer, but this could not be determined due to poor video resolution. In order to corroborate readings between different volunteers who recorded slightly different vehicle arrival times due to streaming lag, car colour was also recorded – but this is not noted in Table 2 as it is not relevant to seismic observations.

As per Table 2, no moving vehicles were noted at 14:46 UTC, when the ORX signal was detected.

A truck which passed the camera at 14:47 UTC was identified in the seismic dataset as being a source of noise beginning at 14:45:50 UTC, and extending out to 14:49 UTC. Given this long duration, and its slow speed observed in the video data, we suspect it was idling in the layby prior to driving away.

Summary

Seismic signatures associated with the EDL of the OSIRIS-REx spacecraft were recorded by an 11-instrument seismic array located almost immediately under the point of peak heating over northern Nevada.

A classic rounded N-wave, characteristic of a decayed sonic boom, is observed propagating across the array. The entire N-wave (compression and rarefaction) lasts approximately 0.2 s, with the compressional wave extending to higher frequencies (up to at least ~450 Hz) than the rarefaction (~40 Hz). The measured duration of the N-wave is in good agreement (within a factor 2) with theoretical predictions.

The wavefront’s moveout across the array is predominantly in the downrange direction (at an azimuth of 253°, close to the pre-landing prediction of 249°. The wave is also propagating almost vertically downward (around 4° from the vertical). Following the N-wave, a set of seismic post-cursors are recorded, likely some combination of air-coupled seismic waves, additional (slower) airwaves, and long-period ground deformation induced by the initial wavefront.

Data from this array are able to exclude the spacecraft being well south of its nominal trajectory. Analysis of the apparent slowness of the N-wave across the array also indicates an equivalent point-source origin which is almost exactly overhead in both the uprange-downrange and cross-range planes.

Further work would likely enable a more thorough inversion of the capsule’s trajectory, accounting for the extended nature of the source and the effects of refraction arising from atmospheric stratification. This would enable this dataset to be used as a more reliable test-case for trajectory determinations of natural meteoroids using their seismic signatures.

Data and Resources

Seismic data, instrument responses, deployment locations and ancillary data (weather and traffic data) are available via in this Zenodo repository: <https://doi.org/10.5281/zenodo.12210877>. [Link will go live once paper is through review, so that if any additional information is needed in the repository we can add it.]

Declaration of Competing Interests

The authors acknowledge that there are no conflicts of interest recorded.

Acknowledgments

The authors are most grateful to NASA’s Scientifically Calibrated In-Flight Imagery (SCIFLI) team for facilitating the fieldwork component of this expedition and to the townspeople of Eureka, Nevada for their hospitality. They are also grateful to NVDOT for the free access to traffic and meteorological data.

BF is funded by the Blaustein Fellowship in Earth and Planetary Sciences at Johns Hopkins University. JW was funded by the Miller

TABLE 2.

Traffic data recorded by the cameras at the US 50 Bean Flat Rest Area. Note that 'Away' and 'Towards' refer to whether the vehicle was moving away from (westbound) or towards (eastbound) relative to the westward-facing traffic camera. Speeds were judged by each individual relative to the average in the 30 minutes or so preceding the interval of interest

UTC Time - Lower Bound	UTC Time - Mean	UTC Time - Upper Bound	Direction	Speed	Type
14:39:26	14:39:47	14:40:03	Away	Medium/Fast	Car
14:41:23	14:41:35	14:41:53	Towards	Medium	Car (with trailer?)
14:41:38	14:41:39	14:41:38	Towards	Medium	Car (with trailer?)
14:47:49	14:47:57	14:48:00	Away	Slow/stationary	Lorry/truck
14:51:47	14:51:52	14:52:00	Towards	Medium/Slow	Car with trailer

472 Institute for Basic Research in Science at UC Berkeley. CC is funded
473 by the UK Space Agency Fellowship in Mars Exploration Science
474 under ST/Y005600/1. TC thanks the Royal Society for funding
475 under URF\R\231019.

References

- 476 Ajluni, T., D. Everett, T. Linn, R. Mink, W. Willcockson, and
477 J. Wood (2015). OSIRIS-REx, returning the asteroid sample. In
478 *2015 IEEE aerospace conference*, pp. 1–15. IEEE.
- 479 Allander, K. K. and D. L. Berger (2009). Seismic velocities and
480 thicknesses of alluvial deposits along Baker Creek in the Great
481 Basin National Park, east-central Nevada. Technical report, U.
482 S. Geological Survey.
- 483 Ben-Menahem, A. and S. J. Singh (1981). *Seismic waves and sources*.
484 Springer Science & Business Media.
- 485 Carlson, H. W. and D. J. Maglieri (1972). Review of sonic-boom
486 generation theory and prediction methods. *The Journal of the*
487 *Acoustical Society of America* **51**(2C), 675–685.
- 488 Cates, J. E. and B. Sturtevant (2002). Seismic detection of sonic
489 booms. *The Journal of the Acoustical Society of America* **111**(1),
490 614–628.
- 491 Cook, J. C. and T. T. Goforth (1970). Ground motion from sonic
492 booms. *Journal of Aircraft* **7**(2), 126–129.
- 493 Edwards, W. N., D. W. Eaton, and P. G. Brown (2008). Seismic
494 observations of meteors: Coupling theory and observations.
- 495 Fernando, B., C. Charalambous, C. Saliby, E. Sansom, C. Larmat,
496 D. Buttsworth, D. Hicks, R. Johnson, K. Lewis, M. McCleary,
497 et al. (2024). Seismoacoustic measurements of the OSIRIS-REx
498 re-entry with an off-grid Raspberry PiShake. *Seismica* **3**(1).
- 499 Fernando, B., N. Wójcicka, M. Froment, R. Maguire, S. C. Stähler,
500 L. Rolland, G. S. Collins, O. Karatekin, C. Larmat, E. K. Sansom,
501 et al. (2021). Listening for the landing: Seismic detections of
502 Perseverance's arrival at Mars with InSight. *Earth and Space*
503 *Science* **8**(4), e2020EA001585.
- 504 Fernando, B., N. Wójcicka, Z. Han, A. Stott, S. Ceylan,
505 C. Charalambous, G. S. Collins, D. Estévez, M. Froment,
506 M. Golombek, et al. (2021). Questions to Heaven. *Astronomy*
507 *& Geophysics* **62**(6), 6–22.
- 508 Fernando, B., N. Wójcicka, R. Maguire, S. C. Stähler, A. E.
509 Stott, S. Ceylan, C. Charalambous, J. Clinton, G. S. Collins,
510 N. Dahmen, et al. (2022). Seismic constraints from a Mars
511 impact experiment using InSight and Perseverance. *Nature*
Astronomy **6**(1), 59–64.
- 512 Kanamori, H., J. Mori, B. Sturtevant, D. Anderson, and T. Heaton
513 (1992). Seismic excitation by space shuttles. *Shock waves* **2**,
514 89–96.
- 515 Karakostas, F., V. Rakoto, P. Lognonne, C. Larmat, I. Daubar, and
516 K. Miljković (2018). Inversion of meteor rayleigh waves on earth
517 and modeling of air coupled rayleigh waves on mars. *Space*
518 *Science Reviews* **214**, 1–33.
- 519 Kenda, B., M. Drilleau, R. F. Garcia, T. Kawamura, N. Murdoch,
520 N. Compaire, P. Lognonné, A. Spiga, R. Widmer-Schmidrig,
521 P. Delage, V. Ansan, C. Vrettos, S. Rodriguez, W. B. Banerdt,
522 D. Banfield, D. Antonangeli, U. Christensen, D. Mimoun,
523 A. Mocquet, and T. Spohn (2020). Subsurface structure at the
524 insight landing site from compliance measurements by seismic
525 and meteorological experiments. *Journal of Geophysical*
526 *Research: Planets* **125**(6).
- 527 McDonald, J. A. and T. T. Goforth (1969). Seismic effects
528 of sonic booms: Empirical results. *Journal of Geophysical*
529 *Research* **74**(10), 2637–2647.
- 530 Pierce, A. D. and D. J. Maglieri (1972). Effects of atmospheric
531 irregularities on sonic-boom propagation. *The Journal of the*
532 *Acoustical Society of America* **51**(2C), 702–721.
- 533 Plotkin, K. J. (2002). State of the art of sonic boom modeling. *The*
534 *Journal of the Acoustical Society of America* **111**(1), 530–536.
- 535 ReVelle, D. and W. Edwards (2007). Stardust—an artificial, low-
536 velocity “meteor” fall and recovery: 15 January 2006. *Meteoritics*
537 *& Planetary Science* **42**(2), 271–299.
- 538 ReVelle, D., W. Edwards, and T. Sandoval (2005). Genesis—an
539 artificial, low velocity “meteor” fall and recovery: September 8,
540 2004. *Meteoritics & Planetary Science* **40**(6), 895–916.
- 541 Rost, S. and C. Thomas (2002). Array seismology: Methods and
542 applications. *Reviews of geophysics* **40**(3), 2–1.
- 543 Sansom, E. K., H. A. Devillepoix, M.-y. Yamamoto, S. Abe,
544 S. Nozawa, M. C. Towner, M. Cupák, Y. Hiramatsu,
545 T. Kawamura, K. Fujita, et al. (2022). The scientific observation
546 campaign of the Hayabusa-2 capsule re-entry. *Publications of*
547 *the Astronomical Society of Japan* **74**(1), 50–63.
- 548 Silber, E. A., D. C. Bowman, and S. Albert (2023). A review of infra-
549 sound and seismic observations of sample return capsules since
550 the end of the Apollo era in anticipation of the OSIRIS-REx
551 arrival. *Atmosphere* **14**(10), 1473.

554 Silber, E. A., D. C. Bowman, C. G. Carr, D. P. Eisenberg, B. R. Elbing,
555 B. Fernando, M. A. Garcés, R. Haaser, S. Krishnamoorthy, C. A.
556 Langston, et al. (2024). Geophysical observations of the 24
557 September 2023 OSIRIS-REx sample return capsule re-entry.
558 *arXiv preprint arXiv:2407.02420*.

559 Sorrells, G. G. (1971). A preliminary investigation into the relation-
560 ship between long-period seismic noise and local fluctuations in
561 the atmospheric pressure field. *Geophysical Journal of the Royal*
562 *Astronomical Society* **26**(1-4), 71–82.

563 Whitham, G. B. (1974). *Linear and nonlinear waves*. John Wiley &
564 Sons.

565 Yamamoto, M.-y., Y. Ishihara, Y. Hiramatsu, K. Kitamura, M. Ueda,
566 Y. Shiba, M. Furumoto, and K. Fujita (2011). Detection of acous-
567 tic/infrasonic/seismic waves generated by hypersonic re-entry
568 of the HAYABUSA capsule and fragmented parts of the space-
569 craft. *Publications of the Astronomical Society of Japan* **63**(5),
570 971–978.

571

Manuscript Received 00 July 2024